Available online at www.sciencedirect.com
SCIENCE DIRECT
Journal of Catalysis 237 (2006) 143–151
JOURNAL OF CATALYSIS
www.elsevier.com/locate/jcat

Skeletal Ni catalysts prepared from Ni–Al alloys rapidly quenched at different rates: Texture, structure and catalytic performance in chemoselective hydrogenation of 2-ethylanthraquinone

Huarong Hu [a], Fuzhong Xie [a], Yan Pei [a], Minghua Qiao [a,*], Shirun Yan [a], Heyong He [a], Kangnian Fan [a,*], Hexing Li [b], Baoning Zong [c], Xiaoxin Zhang [c]

[a] *Department of Chemistry and Shanghai Key Laboratory of Molecular Catalysis and Innovative Materials, Fudan University, Shanghai 200433, PR China*
[b] *Department of Chemistry, Shanghai Normal University, Shanghai 200234, PR China*
[c] *Research Institute of Petroleum Processing, Beijing 100083, PR China*

Received 2 August 2005; revised 27 October 2005; accepted 1 November 2005

Abstract

Skeletal Ni catalysts (RQ Ni) prepared by alkali leaching of rapidly quenched Ni–Al alloys have been systematically characterized, focusing on the effect of the cooling rate during alloy preparation. It is found that the residual Al content, texture, structure, surface hydrogen species, and active sites of the RQ Ni catalysts can be controlled by the cooling rate of the Ni–Al alloys. In liquid-phase hydrogenation of 2-ethylanthraquinone (eAQ), the RQ Ni catalyst with higher cooling rate favors hydrogenation of the carbonyl group and retards the saturation of the aromatic ring and the formation of the degradation products, thus leading to a higher yield of H_2O_2. Based on the characterizations, the improved selectivity is ascribed to the dominant population of strongly chemisorbed hydrogen, which is inactive for the hydrogenation of the aromatic ring, along with the electronic interaction between residual metallic Al and Ni, favoring a carbonyl group-bonded configuration of eAQ on the catalyst.

Keywords: Skeletal Ni; Rapid quenching; Cooling rate; Ni–Al alloy; eAQ; Hydrogenation; H_2O_2

1. Introduction

Since the introduction of the rapid quenching technique in the production of alloys with amorphous or nanocrystalline structure [1], this technique has had a substantial impact on our fundamental understanding of materials synthesis by solidification, as well as on our ability to develop materials for technological applications [2]. In catalysis, rapidly quenched alloys are promising as new catalysts or precursors of new catalysts for specific reactions, because the surface of these alloys is rich in low-coordination sites and defects, which are essential for adsorption and activation of the reactants [3]. However, due to the inherently low surface area of the alloys (∼0.1 $m^2\,g^{-1}$), particular emphasis has been devoted to utilizing the alloys as catalyst precursors rather than as catalysts. It has been found that oxidation–reduction treatment can effectively roughen the alloy surface, thus increasing the active surface area for reaction [4]. Controlled oxidation of one or more constituents in the rapidly quenched alloys is another strategy for preparing supported metal catalysts with unique structure and morphology [5].

Raney-type catalyst precursors, with $Ni_{50}Al_{50}$ alloy as a representative, are conventionally solidified naturally. Al, in the form of intermetallic compounds or eutectic, is leached by alkali, and then porous catalysts with surface areas as high as ∼100 $m^2\,g^{-1}$ are obtained [6]. Incorporation of the rapid quenching technique to the preparation of the Raney-type alloys is expected to retain the merits of the rapidly quenched alloys, while circumventing the drawback of low surface area. Recently, several works have revealed that RQ Ni catalysts prepared by alkali leaching of rapidly quenched Ni–Al alloys (RQ Ni–Al) have surface areas comparable to that of Raney

* Corresponding authors. Fax: +86 21 65642978.
E-mail addresses: mhqiao@fudan.edu.cn (M. Qiao), knfan@fudan.edu.cn (K. Fan).

0021-9517/$ – see front matter
doi:10.1016/j.jcat.2005.11.001

Ni [7–10]. More notably, the composition, texture, and structure, and consequently the activity and selectivity, of the RQ Ni catalyst deviate markedly from Raney Ni [10]. Nonetheless, to the best of our knowledge, no work addressing the effect of the cooling rate on the textural and structural properties of the RQ Ni catalyst has been reported to date. In this paper we demonstrate that the physicochemical properties of the RQ Ni catalyst can be adjusted smoothly by changing the cooling rate of the starting Ni–Al alloy as the preparation variable, which offers an efficient but facile way to tailor the catalytic behavior of the RQ Ni catalyst.

2. Experimental

2.1. Preparation of the RQ Ni–Al alloys

The rapidly quenched $Ni_{50}Al_{50}$ alloys solidified at different cooling rates were prepared by a single-roller melt-spinning technique in argon atmosphere. Metallic Ni and Al powders with the weight ratio of 50/50 were melted at 1573 K in an induction furnace for a sufficient time to ensure homogeneity of the melt. The RQ Ni–Al alloy in the form of ribbons was obtained by spraying the melt onto a high-speed water-cooled copper wheel. By changing the rotation speed of the copper wheel, the cooling rate of the RQ Ni–Al alloy was changed accordingly. Because the cooling rate ($\mathrm{d}T/\mathrm{d}t$) cannot be measured directly, it is usually estimated from the rotation speed based on the equation

$$\frac{\mathrm{d}T}{\mathrm{d}t} = \frac{\Delta T \kappa}{y_c L^2},$$

where ΔT is the temperature difference between the melt and the copper wheel; κ is the thermal diffusivity of the sample, with a value of $\sim 0.3\ \mathrm{cm^2\,s^{-1}}$ on the highly conductive copper substrate; y_c is the dimensionless variable, with typical magnitude of ~ 3; and L is the thickness of the ribbon [2]. RQ Ni–Al alloys with cooling rates of ca. 1.8×10^7, 2.5×10^7, 3.2×10^7, 4.7×10^7, and $6.5 \times 10^7\ \mathrm{K\,s^{-1}}$ were prepared; these are designated as RQ Ni–Al1, RQ Ni–Al2, RQ Ni–Al3, RQ Ni–Al4, and RQ Ni–Al5, respectively. The ribbons were additionally embrittled in hydrogen atmosphere at 873 K for 2 h to ease pulverization. The 200-mesh fraction was used throughout the experiments.

2.2. Preparation of the RQ Ni catalysts

The RQ Ni catalysts were prepared by alkali leaching of the rapidly quenched Ni–Al alloys similar to Raney Ni. One gram of RQ Ni–Al alloy was added to 10 ml of 6 M NaOH aqueous solution at 363 K under gentle stirring. After addition, the mixture was stirred at 363 K for 1 h for further alkali leaching. The black powder was washed thoroughly with distilled water to neutrality and then with ethanol to replace water. The resulting catalyst was immersed in ethanol before characterization and activity testing. The as-prepared RQ Ni catalysts are labeled RQ Ni1, RQ Ni2, RQ Ni3, RQ Ni4, and RQ Ni5, in order of increasing cooling rate. It should be emphasized here that because the RQ Ni catalysts are pyrophoric, care must be taken to avoid air oxidation during sample handling.

2.3. Catalyst characterization

The bulk composition of RQ Ni was analyzed by inductively coupled plasma–atomic emission spectroscopy (ICP-AES; Thermo Elemental IRIS Intrepid). The multipoint Brunauer–Emmett–Teller (BET) surface area (S_{BET}) and the pore volume of RQ Ni were determined by N_2 adsorption at 77 K using a Micromeritics TriStar3000 apparatus. Samples were transferred to the adsorption glass tubes with ethanol and treated at 383 K under ultrahigh-pure nitrogen flow for 2 h before measurement. Sample weight was obtained from the difference in the adsorption tube on completion of the experiment.

Powder X-ray diffraction (XRD) was executed on a Bruker AXS D8 Advance X-ray diffractometer using Cu-K_α radiation (0.15418 nm). The tube voltage was 40 kV, and current was 40 mA. RQ Ni with solvent was loaded in the in situ cell, with argon (99.9995%) flow purging the cell during detection to prevent oxidation. The mean crystallite size was calculated from the integral width of the Ni(111) diffraction line using the Scherrer relation after correction for instrumental broadening with the Warren procedure [11]. Estimates of the contribution to any given peak width by the instrumental factor were obtained using quartz powder because of its good crystalline perfection and virtually no intrinsic line broadening [12]. Because nickel is face-centered cubic (fcc), mean unit-cell-parameter evaluations were made from the intraplanar spacings calculated for all observed diffraction peaks using the simple crystallographic relation that holds for cubic structures.

The surface morphology and particle size were obtained from scanning electron microscopy (SEM; Philips XL30). Before being transferred into the SEM chamber, RQ Ni with ethanol was dispersed on the sample holder and quickly moved into the vacuum evaporator in which a thin gold film was deposited after drying in vacuo. Transmission electron microscopy (TEM; JEOL JEM2011) was operated at 200 kV. RQ Ni powders were dispersed in ethanol and sonicated for ~ 1 min. One drop of the suspension was deposited on a specimen grid coated with a holey carbon film.

The surface composition and electronic state of the catalysts were detected by X-ray photoelectron spectroscopy (XPS; Perkin–Elmer PHI5000C). Al-K_α radiation ($h\upsilon = 1486.6$ eV), operated at 250 W and 14.0 kV, was used as the exciting source. The sample was pressed to a self-supported disc and kept in ethanol before being mounted on the sample plate. Before analysis, the sample was degassed in the pretreatment chamber at room temperature for 4 h in vacuo. The C 1s line of contaminant carbon with binding energy (BE) of 284.6 eV was used as the internal standard. For quantitative purposes, the intensity of the photoelectron peak was integrated after subtracting a Shirley-shaped background. The surface composition of the RQ Ni catalyst was calculated from the intensities of the Ni 3p and Al 2p peaks, which have similar probing depths.

The types of active sites present on the RQ Ni catalysts were studied by temperature-programmed desorption of hydro-

Table 1
Physicochemical characters of the RQ Ni catalysts leached from Ni–Al alloys solidified at different rates

Catalyst	Bulk composition (wt%)	Surf. comp.[a] (wt%)	Surf. comp.[b] (wt%)	S_{BET} ($m^2\,g^{-1}$)	V_{pore} ($cm^3\,g^{-1}$)	d_{pore} (nm)	d_{cryst}[c] (nm)	d_{cell}[d] (nm)	S_H[e] ($m^2\,g_{Ni}^{-1}$)
RQ Ni1	$Ni_{82.9}Al_{17.1}$	$Ni_{83}Al_{17}$	$Ni_{88}Al_{12}$	122	0.091	3.0	6.2	0.3547	10
RQ Ni2	$Ni_{82.6}Al_{17.4}$	$Ni_{83}Al_{17}$	$Ni_{86}Al_{14}$	119	0.093	3.1	5.4	0.3551	11
RQ Ni3	$Ni_{81.9}Al_{18.1}$	$Ni_{83}Al_{17}$	$Ni_{85}Al_{15}$	116	0.096	3.3	4.8	0.3553	12
RQ Ni4	$Ni_{81.4}Al_{18.6}$	$Ni_{82}Al_{18}$	$Ni_{83}Al_{17}$	112	0.099	3.5	4.5	0.3556	14
RQ Ni5	$Ni_{80.7}Al_{19.3}$	$Ni_{82}Al_{18}$	$Ni_{82}Al_{18}$	108	0.104	3.7	4.0	0.3558	16

[a] Surface composition including oxidized aluminum.
[b] Surface composition without considering oxidized aluminum.
[c] Mean crystallite size.
[d] Mean unit-cell dimension.
[e] Active surface area derived from hydrogen chemisorption.

gen (H_2-TPD). After the catalyst was treated at 423 K for 1 h under argon flow (99.9995%, deoxygenated by an Alltech Oxy-trap filter), it was cooled to room temperature before saturation chemisorption of hydrogen by pulsed injection as confirmed by the constant eluted peak area. The maximum desorption temperature of 700 K was reached at a ramping rate of 20 K min^{-1}. The H_2 signal (mass 2) was monitored by an on-line mass spectrometer (MS; Stanford SRS200). Active surface area was calculated from the volume of hydrogen desorbed by assuming H/Ni(s) of 1 and a surface area of 6.5×10^{-20} m^2 per Ni atom [13]. Turnover frequency (TOF) was expressed as the number of H_2 molecules consumed on per active surface nickel atom per second by differentiating the H_2 uptake curve and extrapolating to zero reaction time.

2.4. Activity test and product analysis

Liquid-phase hydrogenation of eAQ was carried out in a 220-ml stainless steel autoclave at 323 K, a total pressure of 0.3 MPa, and a stirring rate of 1000 rpm to eliminate the diffusion effect. After being loaded with 0.5 g catalyst, 3.5 g eAQ, and 70 ml of working solution (trioctylphosphate/trimethylbenzene = 3/7, in volume), the autoclave was sealed and purged with hydrogen four times. When the reaction temperature was reached, the stirring was started, which was taken as the beginning of the reaction. The reaction process was monitored by sampling the reaction mixture at intervals for O_2 oxidation. The H_2O_2 produced was extracted by distilled water and separated from the organic layer. The water layer was titrated by $KMnO_4$ in acidic solution. The percent yield of H_2O_2 (X) is expressed as the ratio of the moles of H_2O_2 to the initial moles of eAQ in the reactor, that is, $X = n^t_{H_2O_2}/n^0_{eAQ} \times 100\%$. The organic layer was analyzed by high-performance liquid chromatography (HPLC; Hewlett–Packard HP1100). eAQ and 2-ethyltetrahydroanthraquinone (H_4eAQ) can be readily quantified by HPLC with an ultraviolet detector using a Zorbax column (ODS, 15 cm × 4.6 mm) with an accuracy of 5%.

3. Results and discussion

3.1. Bulk composition and texture

The evolutions of the bulk composition, BET surface area, pore volume, and mean pore diameter of the RQ Ni catalysts against the cooling rate are summarized in Table 1. After alkali leaching, the amount of Ni increases from 50 wt% in the original alloys to >80 wt%; that is, >75% of Al has been dissolved. Table 1 further reveals that with an incremental rise in the cooling rate, the residual Al in the RQ Ni catalysts increases gradually, suggesting that the improved cooling rate does not favor the leaching of Al [10]. The effects of residual Al on the texture of the RQ Ni catalysts are twofold. On one hand, it leads to a lower surface area as fewer pores due to Al dissolution are generated, which is manifested by the monotonous decrease in the BET surface area from 122 $m^2\,g^{-1}$ for RQ Ni1 to 108 $m^2\,g^{-1}$ for RQ Ni5. On the other hand, a portion of residual Al in the form of Ni_2Al_3, as elucidated by XRD patterns discussed later in the paper, can stabilize the skeleton of the catalysts [14], accounting for the increased pore volume and pore diameter from RQ Ni1 to RQ Ni5. In addition, the RQ Ni catalysts have similar N_2 adsorption–desorption isotherms and pore size distribution curves (not shown here), implying that the cooling rate does not affect the pore structure of the RQ Ni catalysts.

3.2. Phase composition and unit-cell parameter

Fig. 1 reveals that besides the diffraction peaks associated with the (111), (200), and (222) planes of fcc Ni, there are peaks corresponding to the (110), (202), and (212) planes of the Ni_2Al_3 phase for the RQ Ni catalysts [15]. The existence of a residual Ni_2Al_3 phase when leaching similarly quenched Ni–Al [9] and Ni–P–Al alloys [7] has been noted. Further inspection of Fig. 1 reveals that the intensity of the Ni_2Al_3(110) peak surpasses that of the Ni(111) peak for RQ Ni5, while they overlap for RQ Ni1. This phenomenon is consistent with the chemical analysis result that the higher cooling rate leads to more residual Al in the leached catalysts.

The mean crystallite size and unit-cell parameter of the RQ Ni catalysts determined from the diffraction peaks are compiled in Table 1. The crystallites reduce in size with increasing cooling rate, which follows the trend observed for the starting Ni–Al alloys. On the other hand, it is noteworthy that the unit-cell parameters of the RQ Ni catalysts (i.e., the Ni–Ni distance) can be changed by manipulating the cooling rate, with the resulting expected profound impact on the catalytic behavior of the skeletal Ni catalysts. The expansion of the unit cells of the RQ

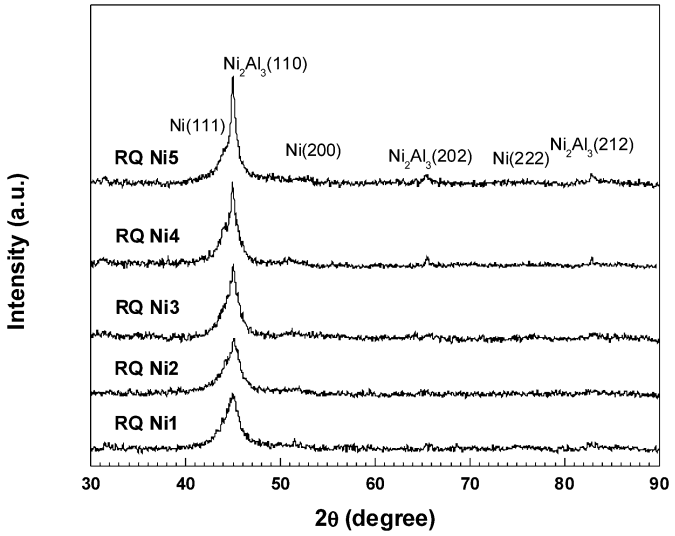

Fig. 1. XRD patterns of the RQ Ni catalysts leached from rapidly quenched Ni–Al alloys solidified at different rates.

Ni catalysts has been interpreted previously as resulting from more confined relaxation of the Ni atoms at a faster cooling rate, leading further deviation of Ni atoms from the equilibrated position, as in Raney Ni (0.3528–0.3535 nm) [12] and pure metallic Ni crystal (0.35268 nm) [16]. An alternative explanation may be that the expansion is caused by defects introduced by rapid quenching. It is known that the higher the cooling rate, the more the defects of the melt are retained in the solidified Ni–Al alloy [3], which is further carried over to the resulting RQ Ni catalyst. Recent atomically resolved STM images of surface defects on Ru(0001) have shown regions with lattice expansion of up to 10% in the immediate vicinity of the defects [17]. Because these two situations have the same origin, it is difficult to distinguish them from each other for the time being.

3.3. Morphology and microstructure

Fig. 2a is a typical SEM image of the RQ Ni–Al alloy that clearly shows the smooth, nonporous surface of the alloy before alkali leaching. The surface is coarsened after alkali leaching, as shown in Figs. 2b–2f for the RQ Ni catalysts. Moreover, the particles of the RQ Ni catalysts exhibit round contours, in contrast to the angular morphology in Raney Ni prepared from the naturally solidified Ni–Al alloy [18]. Comparison of the particles in Figs. 2b–2f leads to the conclusion that a higher cooling rate produces a smaller particle size; the average particle size is ca. 4 μm for RQ Ni1 and decreases continuously to ca. 0.6 μm for RQ Ni5.

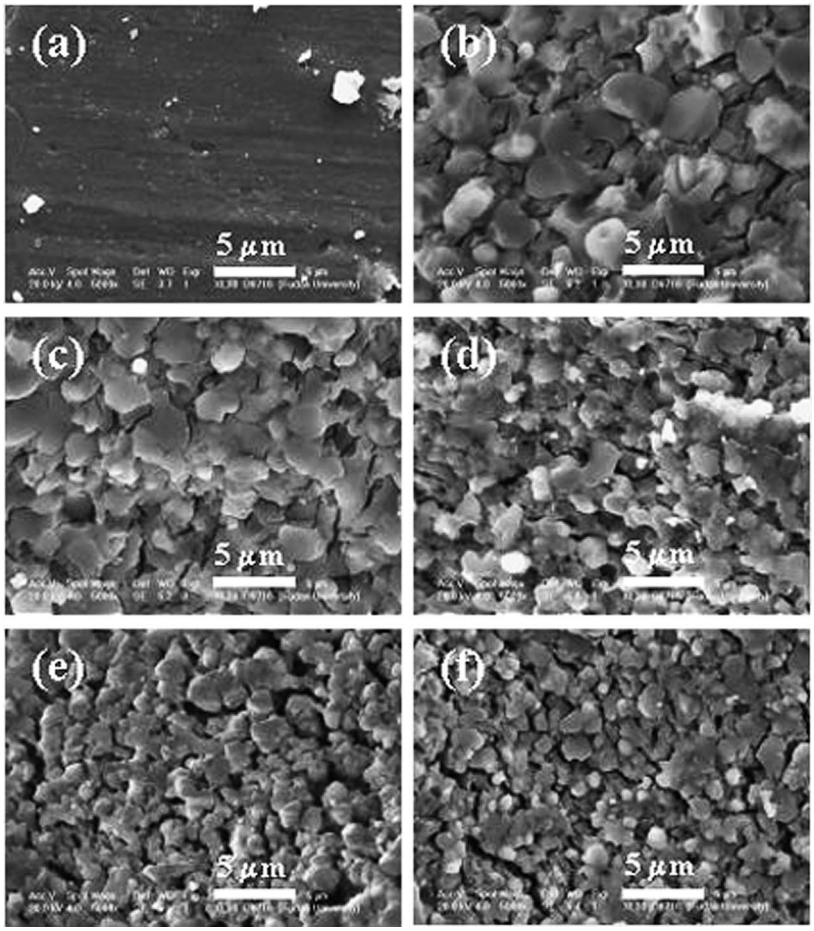

Fig. 2. SEM images of (a) RQ Ni–Al5 alloy, (b) RQ Ni1, (c) RQ Ni2, (d) RQ Ni3, (e) RQ Ni4, and (f) RQ Ni5 catalysts.

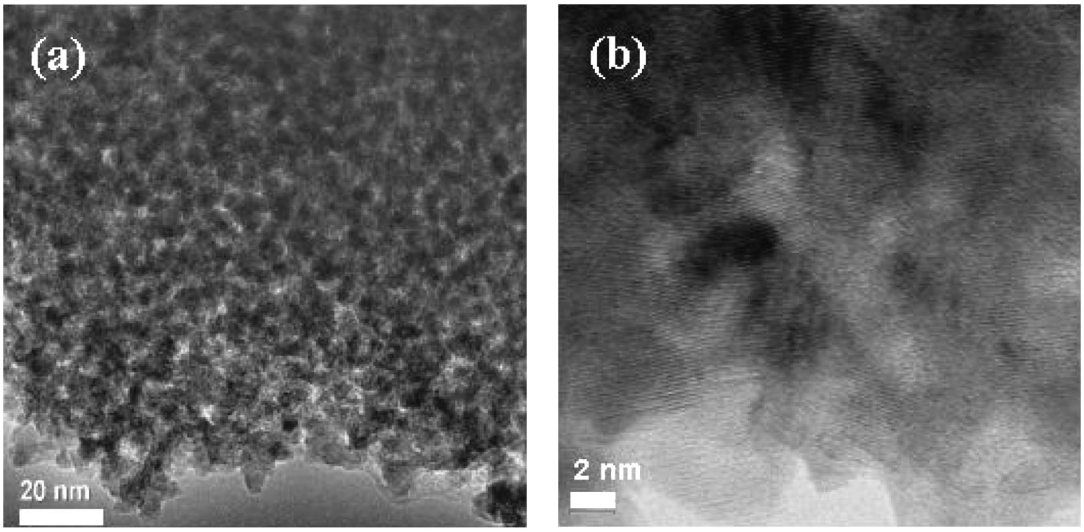

Fig. 3. TEM images of the RQ Ni5 catalyst: (a) low magnification and (b) high magnification.

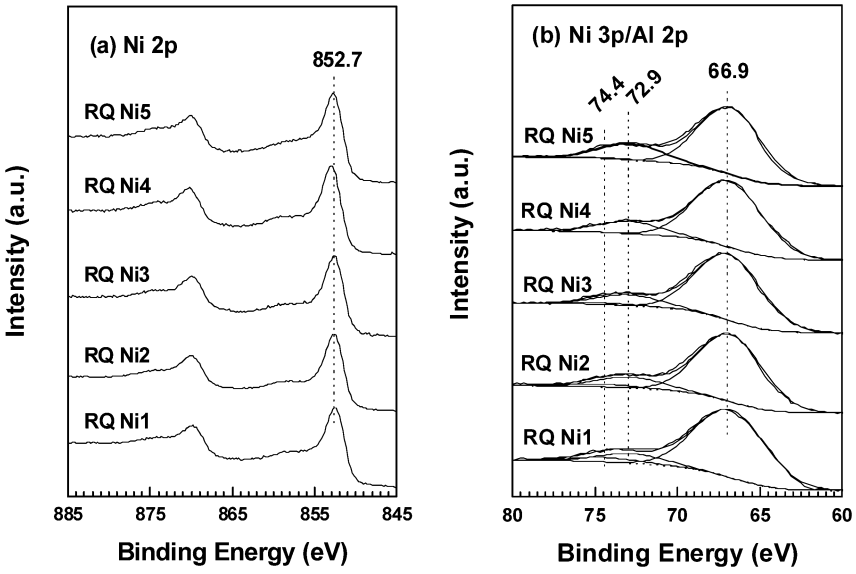

Fig. 4. XPS spectra of (a) Ni 2p and (b) Ni 3p/Al 2p levels of the RQ Ni catalysts.

The low-magnification TEM image shown in Fig. 3a further discloses that the particles in the SEM images consist of even smaller primary crystallites, as is verified by the high-resolution TEM image in Fig. 3b. The mean crystallite size measured from the TEM images is ∼6 nm, quite close to the value calculated from X-ray line broadening. The intraplanar distance measured from the lattice fringes in Fig. 3b is ca. 0.205 nm, attributable to the (111) plane of fcc Ni with a slightly expanded lattice [15]. Fig. 3a clearly shows the homogeneous interparticle/intracrystallite mesopores with diameters of 2–4 nm, close to the pore diameters derived from nitrogen physisorption.

3.4. Surface species and electronic properties

The XPS spectra of the Ni 2p and Ni 3p/Al 2p levels for the RQ Ni catalysts are depicted in Fig. 4. Fig. 4a shows only one Ni $2p_{3/2}$ peak at 852.7 eV assignable to metallic nickel for all catalysts [19]. There is essentially no oxidized nickel species on the RQ Ni catalysts, consistent with the observations of Fouilloux [20] and Delannay et al. on Raney Ni [21], but different than the observations of other authors on RQ Ni [9] and Raney Ni [22–24], most likely due to partial oxidation of metallic Ni during sample handling, because the skeletal Ni catalysts are vulnerable to oxidation.

Because the Al 2p level partially overlaps the Ni 3p level, the Ni 3p/Al 2p spectra were deconvoluted for qualification and quantification purposes. After curve fitting, Fig. 4b reveals two chemical states of Al: metallic Al with BE of 72.9 eV and oxidized Al with BE of 74.4 eV [19], with the most of the Al (>∼70%) in the metallic state. Based on the XRD patterns in Fig. 1, the former is attributed to Al in residual Ni_2Al_3 phase, and the latter to alumina trihydrate adsorbed on the porous skeletal Ni catalysts [6].

From the present Ni 2p and Al 2p spectra, we are unable to distinguish whether or not electron donation between metallic Al and Ni has occurred. Based on magnetic susceptibility, Martin and Fouilloux suggested a donor effect of metallic Al to Ni in Raney Ni [25]. It is most likely that the broad line shape of the Ni 2p and Al 2p levels shadows such interaction.

The surface compositions with and without oxidized Al, calculated from the intensities of the Ni 3p and Al 2p peaks, are summarized in Table 1. The surface compositions including oxidized Al (column 3) are close to the bulk compositions, suggesting no obvious surface segregation of either Ni or Al. In contrast, the surfaces of Raney Ni and its precursor are reportedly enriched with metallic and oxidized Al [22,24,26]. It is also noted that the surface compositions excluding oxidized Al corroborate well with the more intensive Ni_2Al_3 diffractions at higher cooling rates.

3.5. Surface hydrogen species or active site

To obtain information about the dependence of surface hydrogen species or active sites on the cooling rate, H_2-TPD profiles were acquired for all of the catalysts; these are plotted in Fig. 5. In the temperature range 300–700 K, these catalysts are characterized by two hydrogen desorption peaks with desorption maxima of ∼408 and 507 K, indicating the existence of two kinds of adsorption states for hydrogen. The desorption temperatures of hydrogen on RQ Ni catalysts are identical with those on Raney Ni [27]. Following Mikhailenko et al. [28], we attribute the low-temperature peak to weakly chemisorbed hydrogen and the high-temperature peak to strongly chemisorbed hydrogen. Both of these hydrogen species are reversibly adsorbed on the catalyst and are catalytically reactive.

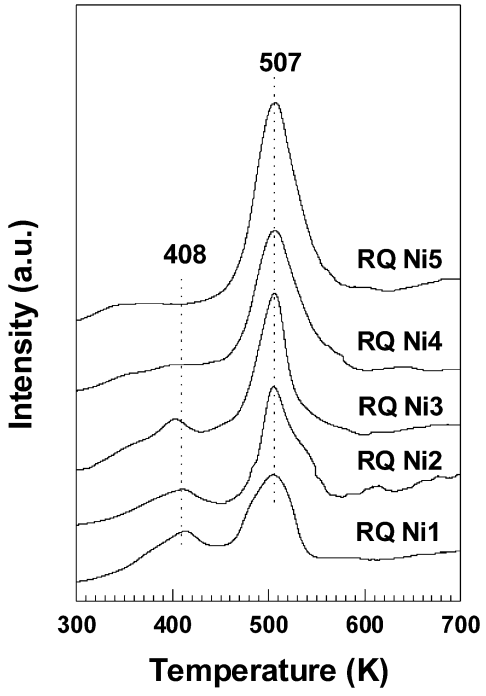

Fig. 5. H_2-TPD profiles of the RQ Ni catalysts.

Although two kinds of surface adsorption sites for hydrogen are always present on the RQ Ni catalysts, the cooling rate alters the concentration of these sites. For RQ Ni1, Fig. 5 shows that the intensity ratio between the peaks at low and high temperatures is about 1:2. With increased cooling rate, the low-temperature peak is attenuated. On the RQ Ni5 catalyst with the highest cooling rate, the weakly chemisorbed peak becomes almost indiscernible. This finding may be used to purposely adjust the selectivity in certain reactions over the RQ Ni catalysts by changing the cooling rate during alloy preparation; previous work has demonstrated that the types of surface hydrogen species are closely related to the catalytic behavior of the Ni-based catalysts [27–32].

The evolution of the population of the weakly and strongly chemisorbed hydrogen should provide an indication of the changes in the microstructure of the RQ Ni catalysts. As discussed in Section 3.2, the RQ Ni catalyst becomes more defective at higher cooling rates. The defects, which are coordinatively unsaturated, tend to bind strongly with hydrogen. This is analogous to the result of the theoretical calculation of hydrogen on Ni(210) surface with low-coordination step sites [33]. Bhatia and Sholl reported that the most energetically favorable adsorption configuration of hydrogen on the Ni(210) surface can be 1.5–5.5 kcal mol_H^{-1} more stable than those on the low-Miller index Ni(100), Ni(111), and Ni(110) surfaces (generally considered the dominant planes on practical Ni catalysts [34]). More interestingly, by modeling surface strain with lattice expansion, Greely et al. found that surface expansion can noticeably improve the stability of surface hydrogen on the Ni(111) surface [35]. This result may be in line with the observation by Heiszman et al. of a considerably increased amount of strongly chemisorbed hydrogen on a Cu-promoted Raney Ni catalyst leached from a ternary Ni–Cu–Al alloy, which they attributed to the incorporation of Cu into the nickel lattice [36]. It is noted that the XRD patterns shown in Fig. 1 and the data given in Table 1 unambiguously demonstrate the expansion of the lattice of the RQ Ni catalysts relative to Raney Ni and pure nickel crystal.

3.6. eAQ selective hydrogenation

To demonstrate how cooling rate influences the catalytic behavior of the RQ Ni catalysts, liquid-phase selective hydrogenation of eAQ was chosen as the probing reaction. It is well known that the clearly dominant process for H_2O_2 production is anthraquinone auto-oxidation [37,38]. In this process (Scheme 1), eAQ dissolved in the working solution is cycled between two main steps: (1) eAQ in the working solution is hydrogenated catalytically to “active quinones” (2-ethylanthrahydroquinone, $eAQH_2$, and 2-ethyltetrahydroanthrahydroquinone, H_4eAQH_2), and (2) the “active quinones” are oxidized with an oxygen-containing gas to produce H_2O_2 and simultaneously recover eAQ and H_4eAQ. However, besides the degradation products, such as 2-ethyloctahydroanthrahydroquinone, 2-ethylanthracene, and 2-ethylanthrone [39,40], H_4eAQH_2 may be as well minimized, because it adds to the viscosity of the working solution and the oxidation of H_4eAQH_2 is inherently more difficult

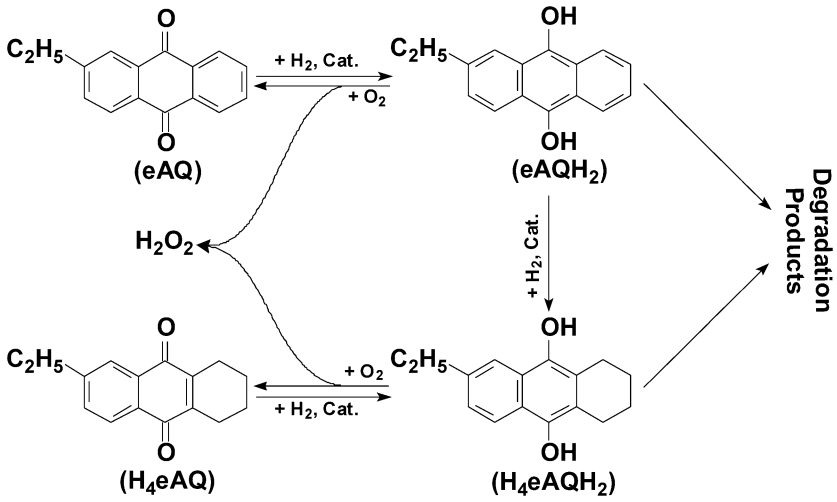

Scheme 1. The hydrogenation and oxidation cycles of eAQ and H_4eAQ.

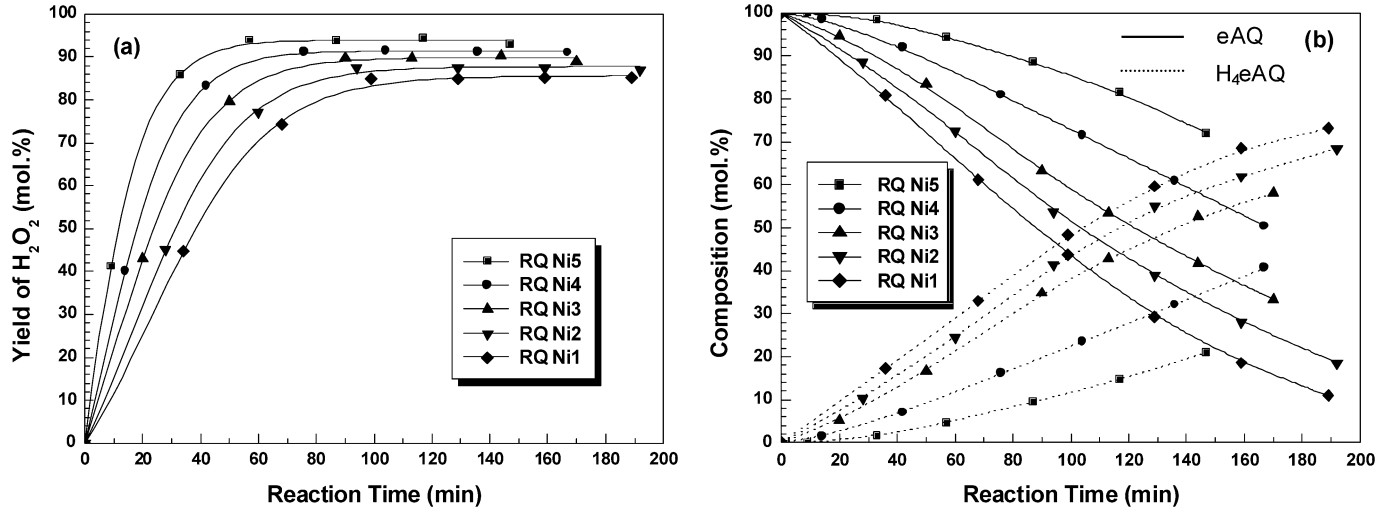

Fig. 6. (a) The percent yield of H_2O_2 and (b) the evolution of eAQ and H_4eAQ after the hydrogenation–oxidation cycle as a function of reaction time over the RQ Ni catalysts.

than that of $eAQH_2$, leading to poor efficiency in H_2O_2 production [41].

Fig. 6a shows the percent yield of H_2O_2 after the hydrogenation–oxidation cycle as a function of reaction time over the RQ Ni catalysts. The reaction times corresponding to the maximum yield of H_2O_2, the catalytic activities expressed in initial hydrogen uptake rates (r_H), and TOF values are summarized in Table 2. It is found that the r_H values over the RQ Ni catalysts increase in the order RQ Ni1 < RQ Ni2 < RQ Ni3 < RQ Ni4 < RQ Ni5. However, such an incremental increase cannot be attributed solely to the enlarged active surface areas (S_H) as listed in Table 1. Table 2 shows that the TOF values also increase, implying that the nature of the active sites has been modified by the varying cooling rate.

An even more attractive finding shown in Fig. 6a is that the maximum yield of H_2O_2 also increases in the same manner. On the RQ Ni1 catalyst, a maximum yield of H_2O_2 of 84.8 mol% is achieved at a reaction time of 97 min, whereas on the RQ Ni5 catalyst, the yield reaches a value as high as 94.0 mol%, about 27 mol% higher than that on Raney Ni [8], while the corresponding reaction time is substantially decreased, to 57 min.

Table 2
Catalytic behavior of the RQ Ni catalysts in eAQ selective hydrogenation

Catalyst	$X_{H_2O_2}$ [a] (%)	t [a] (min)	$Y_{H_4eAQH_2}$ [a] (mol%)	r_H [b] (mmol min^{-1} g_{cat}^{-1})	TOF [b] (s^{-1})
RQ Ni1	84.8	97	48.3	0.316	0.021
RQ Ni2	87.6	94	41.4	0.477	0.029
RQ Ni3	89.8	90	34.8	0.638	0.034
RQ Ni4	91.3	76	17.6	0.887	0.040
RQ Ni5	94.0	57	4.2	1.271	0.052

[a] The maximum yield of H_2O_2 ($X_{H_2O_2}$) and the corresponding reaction time (t) and H_4eAQH_2 yield ($Y_{H_4eAQH_2}$).

[b] Hydrogen uptake rate (r_H) extrapolated to the zero reaction time and the corresponding TOF value.

Referring to Scheme 1, the percent yield of H_2O_2 reflects only the overall hydrogenation selectivity to $eAQH_2$ and H_4eAQH_2. To gain deeper insight into the effect of the cooling rate on the hydrogenation selectivities toward the carbonyl

group and the aromatic ring in eAQ molecule, we monitored the evolution of eAQ and H_4eAQ during the hydrogenation process. Remember that because the chromatographic analysis follows the oxidation step, $eAQH_2$ and H_4eAQH_2 have already been completely converted to eAQ and H_4eAQ, respectively; the detected eAQ represents $eAQH_2$ and unreacted eAQ, whereas H_4eAQ equals H_4eAQH_2 in quantity. Thus the yield of H_4eAQ versus time can be taken as an indirect measure to compare the selectivities to the carbonyl group over different catalysts.

Table 2 and Fig. 6b show that over the RQ Ni1 catalyst, H_4eAQH_2 is generated as soon as hydrogenation commences. At the maximum yield of H_2O_2, 48.3% of eAQ is converted to H_4eAQH_2, suggesting that RQ Ni1 is not selective in the hydrogenation of the carbonyl group. With increased cooling rate, the yield of H_4eAQH_2 at the maximum yield of H_2O_2 decreases accordingly. On the most selective RQ Ni5 catalyst, H_4eAQH_2 does not appear in the first few minutes, and then increases very slowly at prolonged reaction time. On reaching the maximum yield of H_2O_2, the yield of H_4eAQH_2 on RQ Ni5 is only 4.2 mol%, indicating that the hydrogenation of the aromatic ring can be effectively suppressed by improving the cooling rate during alloy preparation.

The superior selectivity of the RQ Ni5 catalyst in eAQ hydrogenation can be directly correlated with the predominant population of the strongly chemisorbed hydrogen. Mikhailenko et al. found that the relative amount of the weakly and strongly chemisorbed hydrogen determines the selectivity in eAQ hydrogenation [28]; this finding is further verified by our work on a RQ Ni catalyst [8] and amorphous nickel boride-based catalysts [42,43], because the weakly chemisorbed hydrogen is highly reactive in aromatic ring hydrogenation, whereas the hydrogenation of the carbonyl group is caused by an electronic mechanism and is limited by hydrogen activation [44]. For comparison, on Raney Ni, about 65% of eAQ has been converted to H_4eAQH_2 when the yield of H_2O_2 reaches the maximum value of only about 67 mol%, which is attributed to the presence of nearly comparable amount of weakly and strongly chemisorbed hydrogen [8]. From Table 2, Fig. 6 and the hydrogenation result on Raney Ni, the additional conclusion can be drawn that the weakly chemisorbed hydrogen is responsible for the formation of the degradation products, which have no contribution to H_2O_2 while they lead to irreversible consumption of "active quinones."

On the other hand, it is suggested that residual Al plays an important role in the performance of Raney-type Ni catalysts, because it can act as an electron donor to nickel, rendering the d-band of nickel less electron deficient and thus influencing the adsorption of the reacting species [20]. In the case of catalytic hydrogenation, it is generally assumed that the reactive bond is that bond involved in chemisorption on the surface [45]. Although we did not resolve electron donation from Al to Ni on XPS, by analogy we suggest that a similar electronic interaction is also present in the RQ Ni catalysts. Due to the enhanced electronic repulsive interaction [46], the electron-enriched Ni is adverse to the adsorption of eAQ in an aromatic ring-bonded configuration, decreasing the likelihood of aromatic ring hydrogenation. Moreover, by a systematic theoretical calculation, Delbecq and Sautet suggested that the main attractive effect in the adsorption of aldehyde on surfaces is the back-donation from the metal orbitals into the π^*_{CO} orbital [46]. In this respect, the electron donation from Al to Ni can enhance such back-donation and consequently favor the bonding using the carbonyl group. We believe that the higher population of the strongly chemisorbed hydrogen and the presence of more residual metallic Al at higher cooling rates are the main factors underlying the higher selectivity in saturating the carbonyl group than the aromatic ring in eAQ hydrogenation.

4. Conclusion

The cooling rate during the preparation of rapidly quenched Ni–Al alloys plays a crucial role in the composition, texture, and structure of the skeletal Ni catalysts and, consequently, on the activity and selectivity in eAQ hydrogenation. Although the geometric and electronic characters and the catalytic behavior of the rapidly quenched catalysts await further elucidation and exploration, the adjustable atomic distance and composition of the rapidly quenched skeletal Ni catalysts are especially attractive for researchers aiming to synthesize tailor-made catalysts. The present study clearly indicates that this tailoring can be achieved by using the cooling rate as the preparation variable.

Acknowledgments

This work is supported by the Major State Basic Research Development Program (grant G2000048009), the National Natural Science Foundation of China (grant 20203004), and the Shanghai Science and Technology Committee (grant 03QB14004).

References

[1] K. Klement, R.H. Willens, P. Duwez, Nature 187 (1960) 869.
[2] M.A. Otooni (Ed.), Elements of Rapid Solidification: Fundamentals and Applications, Springer, Berlin Heidelberg, 1998.
[3] K. Hashimoto, Mater. Sci. Eng. A 226–228 (1997) 891.
[4] T. Katona, Á. Molnár, M. Bartók, Mater. Sci. Eng. A 181–182 (1994) 1095.
[5] Á. Molnár, T. Katona, M. Bartók, K. Varga, J. Mol. Catal. 64 (1991) 41.
[6] J. Freel, W.J.M. Pieters, R.B. Anderson, J. Catal. 14 (1969) 247.
[7] H.X. Li, W.J. Wang, J.F. Deng, J. Catal. 191 (2000) 257.
[8] B. Liu, M.H. Qiao, J.F. Deng, K.N. Fan, X.X. Zhang, B.N. Zong, J. Catal. 204 (2001) 512.
[9] H. Lei, Z. Song, D.L. Tan, X.H. Bao, X.H. Mu, B.N. Zong, E.Z. Min, Appl. Catal. A 214 (2001) 69.
[10] H.R. Hu, M.H. Qiao, S. Wang, K.N. Fan, H.X. Li, B.N. Zong, X.X. Zhang, J. Catal. 221 (2004) 612.
[11] B.E. Warren, J. Appl. Phys. 12 (1941) 375.
[12] S.D. Robertson, R.B. Anderson, J. Catal. 23 (1971) 286.
[13] C.H. Bartholomew, R.B. Pannell, J. Catal. 65 (1980) 390.
[14] M.L. Bakker, D.J. Young, M.S. Wainwright, J. Mater. Sci. 23 (1988) 3921.
[15] PDFMaint Version 3.0, Powder Diffraction Database, Bruker Analytical X-Ray Systems GmbH, 1997.
[16] H.E. Swanson, E. Fuyat, Nat. Bur. Stand. Circ. 1 (1953) 13.
[17] J. Wintterlin, T. Zambelli, J. Trost, J. Greeley, M. Mavrikakis, Angew. Chem. Int. Ed. 42 (2003) 2850.
[18] S.D. Robertson, J. Freel, R.B. Anderson, J. Catal. 24 (1972) 130.

[19] J.F. Moulder, W.F. Stickle, P.E. Sobol, K.D. Bomben, in: J. Chastain (Ed.), Handbook of X-Ray Photoelectron Spectroscopy, Perkin–Elmer, Eden Prairie, MN, 1992.
[20] P. Fouilloux, Appl. Catal. 8 (1983) 1.
[21] F. Delannay, J.P. Damon, J. Masson, B. Delmon, Appl. Catal. 4 (1982) 169.
[22] Y. Okamoto, Y. Nitta, T. Imanaka, S. Teranishi, J. Chem. Soc., Faraday Trans. 1 76 (1980) 998.
[23] F. Hochard-Poncet, P. Dellchère, B. Moraweck, H. Jobic, A.J. Renouprez, J. Chem. Soc., Faraday Trans. 91 (1995) 2891.
[24] B.W. Hoffer, E. Crezee, F. Devred, P.R.M. Mooijman, W.G. Sloof, P.J. Kooyman, A.D. van Langeveld, F. Kapteijn, J.A. Moulijn, Appl. Catal. A 253 (2003) 437.
[25] G.A. Martin, P. Fouilloux, J. Catal. 38 (1975) 231.
[26] R. Holm, S. Storp, J. Electron. Spectrosc. Relat. Phenom. 8 (1976) 139.
[27] M. Serra, P. Salagre, Y. Cesteros, F. Medina, J.E. Sueiras, J. Catal. 209 (2002) 202.
[28] S.D. Mikhailenko, A.B. Fasman, N.A. Maksinova, E.V. Leongard, Appl. Catal. 12 (1984) 141.
[29] T. Uchikoshi, Y. Sakka, S. Ohno, H. Okuyama, K. Yoshihara, Surf. Sci. 287–288 (1993) 1082.
[30] S. Smeds, T. Salmi, L.P. Lindfors, O. Krause, Appl. Catal. A 144 (1996) 177.
[31] J. Estellé, J. Ruz, Y. Cesteros, R. Fernádez, P. Salagre, F. Medina, J.E. Sueiras, J. Chem. Soc., Faraday Trans. 92 (1996) 2811.
[32] M. Serra, P. Salagre, Y. Cesteros, F. Medina, J.E. Sueiras, J. Catal. 197 (2001) 210.
[33] B. Bhatia, D.S. Sholl, J. Chem. Phys. 122 (2005) 204707.
[34] P. Fouilloux, G.A. Martin, A.J. Renouprez, B. Moraweck, B. Imelik, M. Prettre, J. Catal. 25 (1972) 212.
[35] J. Greeley, W.P. Krekelberg, M. Mavrikakis, Angew. Chem. Int. Ed. 43 (2004) 4296.
[36] J. Heiszman, K. Payer, S. Békássy, J. Petró, Acta Chim. (Budapest) 84 (1975) 431.
[37] T. Ulmann (Ed.), Encyclopedia of Industrial Chemistry, vol. A3, VCH, Weinheim, 1989, p. 443.
[38] J.I. Kroschwitz, M. Howe-Grant (Eds.), Kirk–Othmer Encyclopedia of Chemical Technology, fourth ed., vol. 13, Wiley, New York, 1995, p. 961.
[39] A. Drelinkiewicz, J. Mol. Catal. 101 (1995) 61.
[40] A. Drelinkiewicz, M. Hasik, M. Kloc, Catal. Lett. 64 (2000) 41.
[41] E. Santacesaria, M. Di Serio, R. Velotti, U. Leone, J. Mol. Catal. 94 (1994) 37.
[42] X.Y. Chen, S. Wang, J.H. Zhuang, M.H. Qiao, K.N. Fan, H.Y. He, J. Catal. 227 (2004) 419.
[43] J. Fang, X.Y. Chen, B. Liu, S.R. Yan, M.H. Qiao, H.X. Li, H.Y. He, K.N. Fan, J. Catal. 229 (2005) 97.
[44] J.D. Roberts, M.C. Caserio, Basic Principles of Organic Chemistry, W.A. Benjamin, Menlo Park, CA, 1964.
[45] V. Ponéc, Appl. Catal. A 149 (1997) 27.
[46] F. Delbecq, P. Sautet, J. Catal. 152 (1995) 217.